

# Confined Plasmons in Nanofabricated Single Silver Particle Pairs: Experimental Observations of Strong Interparticle Interactions

Linda Gunnarsson, Tomas Rindzevicius, Juris Prikulis, Bengt Kasemo, and Mikael Käll\*

Department of Applied Physics, Chalmers University of Technology, SE-412 96 Göteborg, Sweden

Shengli Zou and George C. Schatz

Department of Chemistry, Northwestern University, 2145 Sheridan Rd., Evanston, Illinois 60208-3113

Received: March 1, 2004; In Final Form: May 27, 2004

We report on the optical properties of single isolated silver nanodisks and pairs of disks fabricated by electron beam lithography. By systematically varying the disk size and surface separation and recording elastic scattering spectra in different polarization configurations, we found evidence for extremely strong interparticle interactions. The dipolar surface plasmon resonance for polarization parallel to the dimer axis exhibited a red shift as the interdimer separation was decreased; as expected from previous work, an extremely strong shift was observed. The scattering spectra of single particles and pairs separated by more than one particle radius can be well described by the coupled dipole approximation (CDA), where the particles are approximated as point dipoles using a modified dipole polarizability for oblate spheroids. For smaller particle separations ( $d < 20$  nm), the simple dipole model severely underestimates the particle interaction, indicating the importance of multipolar fields and finite-size effects. The discrete dipole approximation (DDA), which is a finite-element method, describes the experimental results well even at  $d < 20$  nm, including particles that have metallic bridges.

## 1. Introduction

The brilliant and tunable optical properties of metal nanoparticles have been intensively researched for the past hundred years.<sup>1–4</sup> The key concept in the field of nanoparticle optics is the localized surface plasmon (LSP) resonance, which can be understood as a collective resonant oscillation of all of the conduction electrons of the nanoparticle in response to an incident optical field. A nanoparticle supports a range of LSPs, but the optical response is usually dominated by dipolar modes. The oscillation frequencies are highly dependent on the shape of the nanoparticle, but they also crucially depend on the absolute size and dielectric environment.<sup>5</sup> The oscillation can be localized on a single nanoparticle, or it can involve many coupled nanoparticles. Because of the strong and tunable particle-light interaction, several interesting effects and applications are possible. Examples include surface-enhanced Raman scattering (SERS),<sup>6,7</sup> optical waveguides,<sup>8,9</sup> and biochemical sensors.<sup>10–13</sup>

Recent advances in particle synthesis and nanofabrication technology have made it possible to produce well-defined metal nanostructures, enabling systematic studies of their optical characteristics. A number of groups have studied the optical properties of gold and silver nanoparticle arrays.<sup>14–18</sup> The results show that interparticle coupling effects give rise to pronounced shifts of the LSP resonance frequency compared to isolated particles. Competing factors that give rise to either blue or red shifts with decreasing interparticle distances have been identified.<sup>14,19,20</sup> The electromagnetic coupling between particles involves both very short-distance interactions, due to evanescent fields, and long-range interactions, mainly due to propagating

dipolar fields. A thorough understanding of these local field and coupling effects are crucial for nanoparticle wave-guiding applications, where one wants to achieve efficient energy transport between particles while minimizing far-field scattering losses. Near-field coupling becomes dominant for separations on the order of a particle radius and leads to a strong enhancement of the local electric field in the gap between the particles. This field confinement is believed to be the main contributor to single-molecule SERS, which has been observed by several groups in the past few years.<sup>21–24</sup> It might also lead to strong optical forces directed toward the gap between particles,<sup>25</sup> which might enable optical nanopositioning of molecules for advanced biosensing applications.

To understand the optical coupling between resonant nanoparticles, it is advantageous first to investigate the most basic coupled structure, a pair of particles. Some work in this direction has been reported recently.<sup>26–29</sup> Tamaru et al. investigated single and aggregated colloidal silver particles in a transmission electron microscope (TEM) combined with a far-field scattering setup. They found evidence for a strong interparticle interaction,<sup>28</sup> in agreement with expectations from Mie theory. Similar results were obtained by Prikulis et al.,<sup>29</sup> who used an optical tweezers setup to manipulate individual particles. A different approach was followed by Rechenberger et al.<sup>26</sup> and Su et al.,<sup>27</sup> who used electron beam lithography (EBL) to prepare well-defined gold nanoparticles with varying interparticle separations. The studies showed that there is a continuous red shift in the LSP as the interparticle distance is decreased when the incident light is polarized parallel to the particle pair axis. For light polarized perpendicular to the particle axis, there is instead a weak blue shift of the LSP resonance. This difference is expected from electrodynamic theory, as well as from earlier measurements on particle arrays and lines of particles, and can

\* To whom correspondence should be addressed. E-mail: kall@fy.chalmers.se.

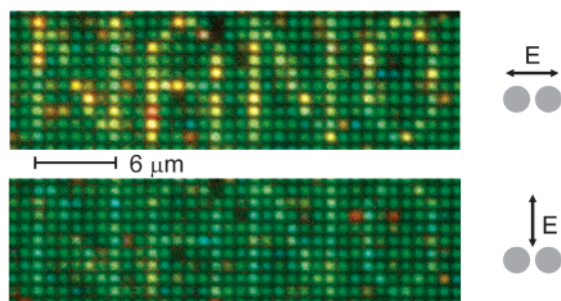


**Figure 1.** Dark-field images form an array of “identical” silver disks with a diameter of 80 nm and a height of 25 nm. The text “NANO” is written with pairs of such particles with an interparticle distance of approximately 110 nm. In the top image, the array is illuminated with light polarized parallel to the particle pair axis. In the bottom image, the polarization is perpendicular to the pair axis.

be interpreted in terms of attractive or repulsive forces created between the induced dipoles due to the coupling.<sup>26</sup> The effect is illustrated in Figure 1, which shows dark-field images of an array of silver particles (80-nm diameter, 25-nm height) in two orthogonal polarization configurations. The text “NANO” is written with pairs of particles with a center-to-center distance of 110 nm. In the upper image, in which the polarization is parallel to the particle pair axis, there is a clear red shift of the LSP compared to the single particles in the greenish background. In the lower image, where the polarization is perpendicular to the pair axis, the LSP is instead slightly blue shifted.

In this work, we use an approach similar to that employed in refs 26 and 27, preparing the structures by electron beam lithography and lift-off. EBL is a powerful tool for creating a wide range of nanoparticle structures, where the size, shape, and arrangement of the nanoparticles can be controlled independently. For features and separations in the 100-nm size range and above, structures can be prepared with high reproducibility. It is possible, though time-consuming, to prepare large arrays of almost identical particles with a low percentage of “stacking faults”. However, for smaller particle features (<100 nm), there will be a nonnegligible spread in the shapes, sizes and interparticle distances of the particles in an array. For closely separated particle pairs, this spread becomes critical because of the strong near-field interaction mentioned above. Gaps smaller than 20–30 nm are hard to achieve and cannot easily be made with high reproducibility. This is the motivation for performing measurements also on single particles and single particle pairs.

The silver particles investigated in this study were prepared on uncoated insulating glass substrates to avoid particle interactions due to propagating surface modes. By arranging particle pairs in arrays with lattice constants of 5 and 1  $\mu\text{m}$ , we were able to measure spectra from single particle pairs and ensembles of approximately 20 pairs, respectively. For the single-pair measurements, we performed scanning electron microscopy (SEM) analysis on exactly the same particle pairs as investigated optically. This approach turned out to be crucial for pairs with small gap sizes, for which metallic contact can occur because of the limited resolution of the EBL. In a similar manner, we also performed a study of single particles with varying diameter. We show that the single-particle plasmon can be tuned over the whole visible spectrum by increasing the diameter of the cylindrically shaped particles. The experimental data were analyzed using a coupled dipole approach and by comparing with simulations based on the discrete dipole approximation (DDA). Both approaches produce results in good agreement with data, although the DDA model is superior for particle pairs with

very small separations. In addition, the DDA method can be used to study particles that have metallic bridges.

## 2. Experimental Section

**2.1. Sample Fabrication.** The samples were prepared by electron beam lithography (EBL) on soda glass substrates. The cleaned glass substrate was first spin coated with a 40-nm-thick film of an electron-sensitive resist (PMMA 950 k), which was then covered with a 10-nm gold film through resistive evaporation in a high-vacuum evaporation system (AVAC HVC 600). The latter step is needed to make the substrate conducting before exposing it to the electron beam, which passes through the gold and exposes the resist as desired. The patterning was performed in a JEOL 9300 XS system, which has a minimum beam size of less than 5 nm.<sup>30</sup> The gold film is then removed by etching in an aqueous solution of 4 g of KI and 1 g of  $\text{I}_2$  in 150 mL of deionized water,<sup>31</sup> after which the pattern can be developed.

The resolution of the pattern is not only set by the diameter of the electron beam but also depends on the resist system and the development procedures in combination with the exposure dose.<sup>32,33</sup> We developed our patterns by dipping the samples in a 9:1 mixture of isopropyl alcohol/water for approximately 60 s, followed by rinsing in deionized water and drying in pure  $\text{N}_2$ . The quality of the development was examined in an optical microscope.

A silver film was then deposited on the patterned resist in the same evaporation system as used before exposure. The deposition rate and thickness were measured throughout the deposition process, and the rate was held constant at approximately 0.5  $\text{\AA}/\text{s}$  to create a smooth film. After deposition, in the lift-off step, the remaining resist and the material on top of it was dissolved in hot acetone. The smallest particle size achieved with the process described above is approximately 20–30 nm.

Some of the structures were also prepared on SiN membranes, which are transparent to electrons and allow for transmission electron microscopy (TEM) analysis. These TEM windows were prepared according to the method described in ref 34 and consist of a 20 nm thin SiN membrane in a  $120 \times 120 \mu\text{m}$  window on an oxidized Si wafer. The windows were patterned and developed following the same scheme as above, but in this case, metalization of the resist film was not needed because the substrate is already conductive.

**2.2. Structural Characterization.** The lateral sizes and shapes of the particles, as well as the interparticle distances for the particle pairs, were mainly determined from SEM images. Because the patterns were prepared on an insulating glass substrate, we had to use a low accelerating power to decrease charging during imaging. This reduced the obtainable resolution. Nonetheless, SEM characterization of both selected individual particles and particle pairs as well as randomly chosen particles in the arrays were carried out, and the particle sizes and interparticle distances could be determined with an accuracy of  $\pm 5$  nm. TEM analysis was also performed on a few structures, and the heights of the particles were usually determined by tapping-mode AFM (DI Nanoscope). Because of the roughness of the particles, the heights were estimated in the 5-nm range. All nanofabrication and characterization steps were performed in the MC2 processlab at Chalmers University of Technology.

**2.3. Optical Characterization.** The optical properties of the silver nanoparticles were examined by elastic light scattering in a dark-field (DF) microscope, as schematically illustrated in Figure 2. Polarized white light is sent through a DF condenser ( $\text{NA} = 0.8\text{--}0.95$ ) toward the sample, which is mounted on a

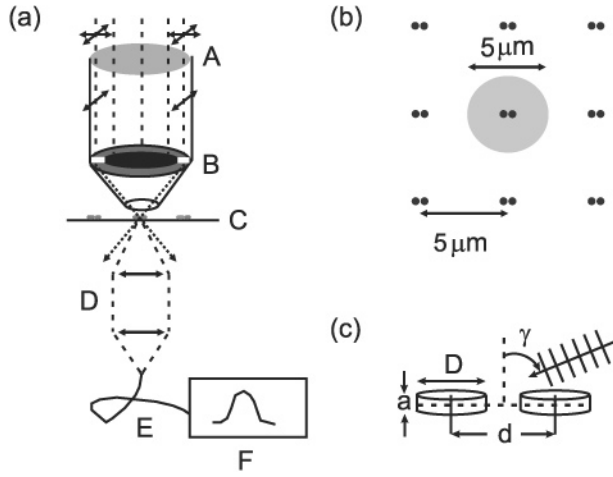


**Figure 2.** (a) Schematic drawing of the dark-field scattering setup. Unpolarized white light is directed toward the sample through a dark-field condenser (NA = 0.8–0.95). The scattered light is collected by a 100× objective, D (Leika, oil immersion, NA = 0.5) and guided through a 400-μm fiber, E, to a spectrometer, F (Avantes S3000). The sample is mounted on a movable and rotatable table, C. On top of the DF condenser there is a polarizer, A, that enables the incoming light to be polarized at a certain angle with respect to the particle pair axis. The polarization is changed by rotating either the sample or the polarizer. Inside the DF condenser, at position B, we sometimes inserted a blocker that only lets light perpendicular to the polarization direction through at the edges. (b) Probed area on an array with a 5-μm grating constant. (c) Pair of oblate spheroids in dark-field setup.  $D$  is the particle diameter,  $d$  is the particle center-to-center separation,  $a$  is the particle height, and  $\gamma$  is the incident field angle to particle plane introduced by the dark-field condenser.

rotatable and movable table. The scattered light is collected by a 100× objective (NA = 0.5) and then guided through a 400-μm fiber connected to a grating spectrometer (Avantes S3000) with a resolution of ~5 nm. A digital color camera enables dark-field imaging. Raw data were corrected by subtracting a background spectrum recorded from a dark area on the substrate and then dividing the result by the white light spectrum from the lamp. Single particles or particle pairs could clearly be seen in the microscope as bright diffraction-limited spots that change color with the particle diameter and interparticle distance. A change in color was also seen when changing the polarization with respect to the particle pair axis, as illustrated in Figure 1.

In the following discussion, parallel polarization and perpendicular polarization imply that incident light is polarized parallel and perpendicular to the particle pair axis, respectively. However, the DF condenser deflects the polarized incident light in such a way that it acquires a polarization component perpendicular to the sample surface. To minimize this contribution, we inserted a blocker, B, that transmits perpendicular to the polarization direction only at the condenser's edges. The blocker did, however, not result in any significant spectral difference, and it was sometimes omitted to improve the signal-to-noise ratio. The measurement area in this setup has a diameter of approximately 5 μm, which means that approximately 20 pairs or single particles contribute to the spectra for arrays with a 1-μm grating constant and only one pair or particle in the 5-μm arrays (see Figure 2b).

### 3. Theoretical Model

The theoretical analysis of the experimental results presented in section 4 is based on solving the coupled dipole equation<sup>40</sup>

$$\mathbf{P}_j = \alpha_j \mathbf{E}_j = \alpha_j (\mathbf{E}_{\text{inc},j} - \sum_{k \neq j} \mathbf{A}_{jk} \mathbf{P}_k) \quad (1)$$

Here,  $\mathbf{P}_j$  represent point dipoles located at positions  $\mathbf{r}_j$ , and the local electric field  $\mathbf{E}_j$  consists of the incident field  $\mathbf{E}_{\text{inc},j} = \mathbf{E}_0 \exp(i\mathbf{k}\mathbf{r}_j - i\omega t)$  and the retarded induced field from all other dipoles.  $\mathbf{A}_{jk}$  is a  $3 \times 3$  matrix (for  $j \neq k$ )

$$\mathbf{A}_{jk} = \frac{\exp(ikr_{jk})}{r_{jk}} \left[ k^2 (\hat{r}_{jk} \hat{r}_{jk} - \mathbf{1}_3) + \frac{ikr_{jk} - 1}{r_{jk}^2} (3\hat{r}_{jk} \hat{r}_{jk} - \mathbf{1}_3) \right] \quad (2)$$

where  $k \equiv \omega/c$ ,  $r_{jk} = |\mathbf{r}_j - \mathbf{r}_k|$ ,  $\hat{r}_{jk} \equiv (\mathbf{r}_j - \mathbf{r}_k)/r_{jk}$ , and  $\mathbf{1}_3$  is the  $3 \times 3$  identity matrix. By defining  $\mathbf{A}_{jj} \equiv \alpha_j^{-1}$ , the scattering problem reduces to a system of  $3N$  complex linear equations

$$\sum_{k=1}^N \mathbf{A}_{jk} \mathbf{P}_k = \mathbf{E}_{\text{inc},j} \quad (3)$$

where  $N$  is the total number of dipoles in the system.

In a first approach, we solve the coupled dipole equation for just two dipoles, representing the particles in a pair. Herein, we refer to this approach as the coupled dipole approximation (CDA). The incident field is chosen so that it essentially mimics the DF setup, i.e.,  $\mathbf{E}_{\text{inc}}$  is a combination of s- and p-polarized light with an angle of incidence that corresponds to the numerical aperture of the DF condenser. Each particle is assigned a polarizability according to the modified long-wavelength approximation (MLWA) for oblate spheroids, as described by Jensen et al.<sup>35</sup>

$$\alpha_{\parallel} = \frac{\alpha}{\left(1 - \frac{2}{3}ik^3\alpha - \frac{k^2}{a}\alpha\right)} \quad (4)$$

Here,  $\alpha$  stands for the electrostatic polarizability of an oblate spheroid

$$\alpha = a^2 c \frac{\epsilon - n^2}{3n^2 + 3L(\epsilon - n^2)} \quad (5)$$

with  $a$  being the major spheroid axis and  $c$  the minor axis. The dielectric function of silver is denoted by  $\epsilon$ , and  $n$  is the refractive index of the surrounding medium.  $L$  is a shape factor given by

$$L_i = \frac{abc}{2} \int_0^\infty \frac{dq}{(s_i^2 + q)\sqrt{(q + a^2)(q + b^2)(q + c^2)}} \quad (6)$$

and  $s_i = a, b, c$ . Because the spheroids are oblate  $a = b$ .

The dipole moments obtained from solving the coupled dipole equation by direct matrix inversion are then used to calculate the scattering cross sections according to

$$C_{\text{sca}} = \frac{8\pi}{3} \frac{k^4}{|\mathbf{E}_{\text{inc}}|^2} (|\mathbf{P}_1|^2 + |\mathbf{P}_2|^2) \quad (7)$$

In the second approach, we use the discrete-dipole approximation (DDA), which was introduced by Devoe<sup>36,37</sup> and extended by Purcell and Pennypacker.<sup>38</sup> The present implementation is derived from Draine and co-workers,<sup>39–41</sup> with revisions by Kelly et al.<sup>5</sup> In brief, the particles and the substrate are



divided into a finite number of polarizable points on a cubic grid that acquire dipole moments because of the local electric field. The scattering problem is specified by assigning the desired polarizability and dipole separation. The coupled dipole equation is then solved by a Fourier transform technique. For a sufficiently small dipole separation, past studies have demonstrated that the DDA method leads to extinction spectra that are nearly exact, i.e., cross sections within 10% of the true value and with the correct wavelength dependence including multipolar and retardation effects.<sup>5</sup>

In the present application, the nanodisks were assumed to be cylindrical, and were divided into elements using a 1.67-nm grid spacing. The substrate effect is modeled using an effective medium approximation that is described by Malinsky et al.<sup>42</sup> in which the dielectric constants of the substrate and ambient (vacuum) are averaged with weight factors that reflect the fractional areas that are exposed to substrate and ambient. Calculations were performed at normal incidence. However, we have recently studied the dependence of the spectra on the  $\mathbf{k}$  vector direction, and we find that changing the incident angle from 0° to 45° has virtually no effect on the spectra, other than an overall scaling of intensities. The present calculations are similar in quality to an earlier DDA study of two-dimensional arrays of disks that had much larger spacings (260–500 nm).<sup>43</sup> In that work, good agreement with the dependence of the measured plasmon wavelengths<sup>15</sup> on array spacing was noted. However, it was noted there, and we also find here, that the plasmon wavelength is slightly shifted from its measured value. This likely arises from slight differences between the actual and idealized shapes of the particles and from substrate interactions that are not quantitatively described by the effective medium model.

## 4. Results and Discussion

**4.1. Single Isolated Silver Disks.** To investigate the variation in LSP position and line shape with particle size, we prepared several sets of single-particle samples by the procedure described in section 2. Particles with the same diameter and height were arranged in square arrays with lattice constants of 5  $\mu\text{m}$ , which is large enough for interparticle interactions to be negligible and for measurements of individual particles to be performed. The particle diameters were varied from 30 to 200 nm. Using dark-field images, it was straightforward to identify specific particles for subsequent SEM analysis, which allowed us to determine the exact particle diameter with an accuracy of  $\pm 5$  nm. The height  $h$  of the particles was estimated by AFM to be in the range of 20–25 nm. The particles were designed to be hexagonal or octagonal in shape, which, at least for the smallest diameters, approximates a circle because of the finite line width of the EBL.

Figure 3a shows scattering spectra of single isolated silver particles with diameters of  $D = 50, 100, 150,$  and  $200$  nm, together with Lorentzian curve fits and calculations based on the MLWA polarizability for oblate spheroids. The intensity axis in Figure 3a is proportional to scattering efficiency, i.e., the absolute scattering intensity for each single particle has been normalized to its geometrical cross section in a plane parallel to the substrate. This allows for convenient comparisons of particles of different sizes and scattering cross sections.

To extract peak positions and line widths, we fitted the experimental data using a Lorentzian form for the particle polarizability  $\alpha$  inserted into the standard equation for the

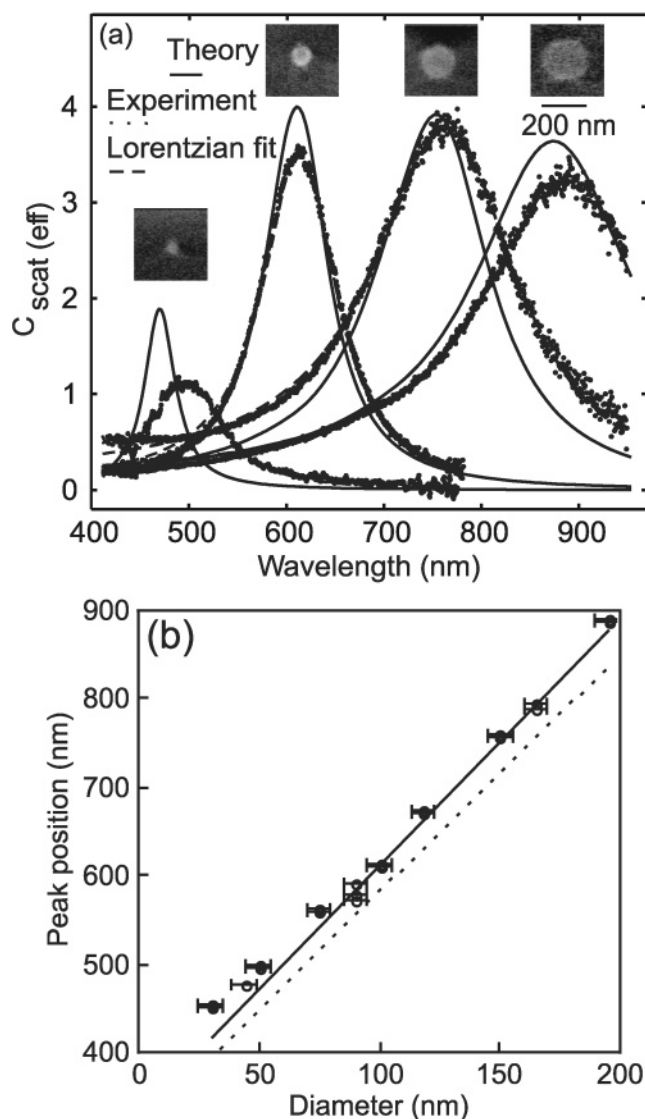


**Figure 3.** (a) Unpolarized dark-field scattering spectra and corresponding SEM images of single isolated particles of different diameters ( $D = 50, 100, 150$  and  $200$  nm). The dashed lines show Lorentzian fits of the experimental data according to eq 8, and solid lines show scattering spectra calculated on the basis of the MLWA polarizability. The experimental and theoretical spectra have been normalized to the geometrical cross section of each particle so that the intensity axis is proportional to the relative scattering efficiency. (b) Experimental LSP position vs particle diameter as determined by SEM analysis. The resolution of the SEM is approximately 10 nm, which is indicated by error bars in the plot. The solid and dashed lines show MLWA results for oblate spheroids with heights of 20 and 25 nm, respectively. The substrate is taken into account through an effective refractive index of 1.25.

scattering cross section,  $\sigma_s \propto k^4 |\alpha|^2$ . The resulting fitting function is

$$I(\lambda) = \frac{I_0}{(\lambda^2 - \lambda_{\text{LSP}}^2)^2 + \lambda^2 \Gamma^2} \quad (8)$$

As can be seen from Figure 3a, eq 8 describes the data very well. Notably, there is no need to include additional inhomogeneous (Gaussian) broadening effects to achieve a good fit. This reflects the fact that the spectra are from single particles, i.e., statistical averaging does not contribute to the line shape. The physical meaning of the Lorentzian response function is that the LSP can be viewed as a damped harmonic oscillator.

Figure 3a also shows calculations of the scattering efficiency using the MLWA polarizability for oblate spheroids, as described in the previous section. In these calculations, the major axis  $a$  is fixed by the measured diameter of each nanodisk,  $D = 2a$ , and the minor axis  $c$  is fixed to the particle height  $h = 2c = 20$  nm. It is obvious that the MLWA model agrees extremely well with the measured spectra for the larger particles, giving very similar resonance positions, line widths, and relative scattering efficiencies. This is somewhat surprising, considering the simplicity of the approach, but well in line with previous results for particle arrays with large lattice constants.<sup>15</sup> The agreement implies that the MLWA can be used to accurately estimate both retardation effects and far-field scattering properties of isolated metal nanoparticles at the limit of the quasistatic regime. For the smallest particle sizes ( $D = 50$  nm), however, the agreement is not as good. The reason for this discrepancy is not clear.

In Figure 3b, we summarize the measured and calculated resonance positions as a function of particle diameter. The graph shows that there is a linear shift of the resonance as a function of particle size, as expected from theory.<sup>4,5</sup> From the slope of the line, we find that the peak position shift is approximately 27 nm per 10 nm change in diameter for the geometry used. The experimental and theoretical slopes agree very well (26.4 and 27.5 nm, respectively). Similar results have been reported for arrays of particles,<sup>44,45</sup> as well as for single Au particles.<sup>27</sup>

In the MLWA calculations, the most important factor that determines the peak position is the aspect ratio  $a/c = D/h$  of the oblate spheroid. This means that the limited accuracy in the height measurement will result in an uncertainty in the exact determination of the resonance position. Specifically, the peak will shift to the blue with smaller aspect ratio, i.e., larger height. This is illustrated by the top and bottom lines in Figure 3b, which correspond to MLWA calculations using  $2c = 20$  and 25 nm, respectively. There is also an uncertainty in the choice of dielectric constant for the medium surrounding the nanoparticle. As in ref 46, we used an effective medium dielectric constant of  $\epsilon_{\text{eff}} = 1.25^2$  obtained from the average refractive indexes of the glass substrate ( $n_{\text{glass}} = 1.5$ ) and the surrounding air ( $n_{\text{air}} = 1.0$ ). This is an approximation, and changing the value of  $\epsilon_{\text{eff}}$  will of course affect the position of the LSP resonance.<sup>42</sup>

We should note that all results above and in the following sections refer to LSP modes polarized in the plane of the disks. The particles should, however, also support modes polarized normal to the disk/substrate. From theory, one expects that these modes, which should occur in the 400-nm wavelength region, would be very weak in the DF illumination configuration used here. This explains why only one mode is observed for each particle size in Figure 3.

**4.2. Particle Pairs.** We prepared pairs of particles with a few different diameters, namely, 50, 80, and 95 nm. The interparticle distances were varied from touching edges to 500-nm center-to-center separation. The smallest gap achieved was approximately 10 nm. For smaller edge-to-edge distances, a bridge connecting the two particles was normally formed. The pairs were prepared in both 1- and 5- $\mu\text{m}$  arrays.

In Figure 4, we show how the LSP wavelength for parallel polarization varies with gap size  $d$  for two different particle diameters,  $D = 80$  and 95 nm. The heights of the particles were approximately 25 nm in both cases, and data were obtained for arrays with a lattice parameter of 1  $\mu\text{m}$ , i.e., each data point represents an average over approximately 20 pairs.

The results in Figure 4 clearly demonstrate that a strong red shift of the scattering peak sets in at  $d \approx D$ . The magnitude of

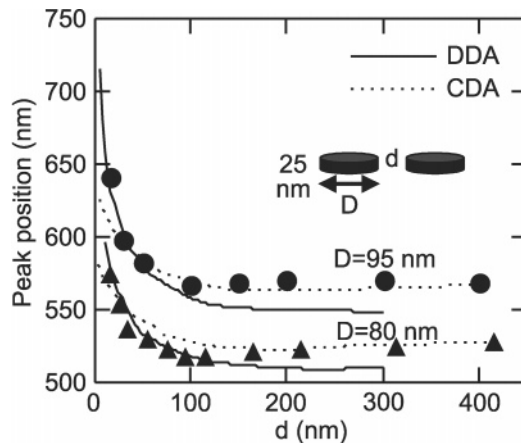


**Figure 4.** LSP peak position for pairs in parallel polarization geometry versus surface separation  $d$ . The particle diameters were  $D = 80$  or 90 nm, and the height was  $h \approx 25$  nm. Each point represents an average over  $\sim 20$  pairs. The full and broken lines show DDA and CDA calculations, respectively, for the same particle and illumination geometry as in the measurements.

the shift, on the order of 10% at the shortest distances, is in quantitative agreement with previous reports on gold particle pairs.<sup>26,27</sup> When the incident light is polarized perpendicular to the pair axis, we instead observe a weak blue shift (not shown), as was also observed by Rechenberger et al.<sup>26</sup> In Figure 4, we also present the results from CDA and DDA calculations on pair arrangements similar to those used in the experiments. The CDA model is based on a particle height of  $h = 20$  nm, which gives the best agreement with single-particle data according to Figure 3b. Both models obviously agree qualitatively with the experimental data. The main discrepancies are that the DDA calculations predict slightly too short LSP wavelengths at large  $d$  values whereas the CDA underestimates the degree of red shift at short distances. The former difference is not surprising given that the DDA particle structure was not optimized to match the single-particle LSP wavelength, as mentioned above. The latter discrepancy is more interesting, as it relates to the essential physics of the interparticle interaction. In the CDA, each particle in the pair is treated as a point dipole, which means that the particle size affects only the coupling via the magnitude of the dipole polarizability  $\alpha(D, h)$ . As the point dipoles are separated by the center-to-center distance  $D + d$ , a surface separation of  $d = 0$  has no particular meaning. The DDA, on the other hand, is a numerical technique that is based on the actual particle separation. This means that near-field coupling effects other than pure particle dipole interactions are automatically included to an accuracy that is essentially given by the spacing of the discrete dipoles that make up each particle in the pair. In particular, the DDA can reproduce the short-range multipolar fields that leads to the diverging behavior seen in Figure 4 when the surface separation approaches  $d = 0$ .

**4.3. Variation between Pairs and Single-Pair Measurements.** In each array discussed above, the particle dimensions and arrangement are designed to be identical. In reality, however, there will always be some variation in the exact size and shape of each particle and, in particular, in the separation between particles. This is clearly seen in Figure 5, which shows TEM micrographs of four different pairs from two separate arrays. Figure 5a–c shows pairs from an array of  $D = 50$  nm particles designed to have a gap of  $d = 10$  nm. This is at the limit of what can be achieved with EBL, and consequently, we observe a considerable spread in gap distances. Most of the particle pairs in this particular array were connected via a bridge,

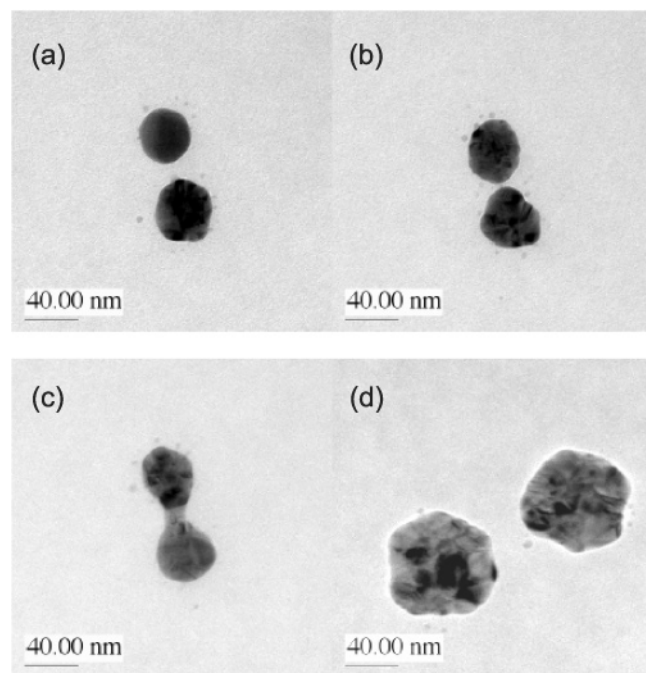


**Figure 5.** TEM micrographs of pairs of particles of two different sizes. Images a–c show pairs of  $D = 50$  nm diameter particles with a surface separation designed to be  $d = 10$  nm. However, the actual gap values are 15 nm in a and 5 nm in b, whereas the pair in c is in contact. The majority of the pairs in this array had a structure similar to that in c. In d, the particle diameter is 80 nm, and the separation is approximately 20 nm. Note the dark and bright areas resulting from polycrystallinity.

as in c, but we also observed pairs separated with gaps varying from (a) 15 to (b) 5 nm.

From the discussion above, we expect that such variation will result in dramatically different LSP positions for the parallel polarization configuration, resulting in a substantial inhomogeneous broadening of ensemble data.

Figure 5d is an image from an array of  $D = 80$  nm,  $d = 30$  nm pairs that clearly reveals darker and lighter areas in the individual particles caused by contrast between Ag crystallites of different orientations. It is not obvious how the polycrystalline nature of the nanoparticles affects their spectral properties. One possibility would be that grain boundaries result in a decreased LSP lifetime, causing spectral broadening. However, the good agreement between measured and calculated line shapes demonstrated in Figure 3a speaks against any pronounced effect.

The high resolution obtained by TEM is, unfortunately, impossible to achieve in our present SEM system, where we probably would have been unable to clearly resolve the difference between particle pairs b and c in Figure 5. Although a slightly more controlled and repeatable particle separation might have been achieved if the EBL fabrication process had been further optimized, for example, with respect to exposure and development times, the TEM images clearly highlight the need for single-pair data at short  $d$  values. Such results are shown in Figure 6, which displays scattering spectra from individual particle pairs measured in the two orthogonal polarization configurations together with corresponding SEM images. The diameter and height of these particles are approximately  $D = 95$  nm and  $h = 25$  nm, respectively, and surface separations vary from 10 to 250 nm. The single-pair spectra exhibit several interesting effects that would have been difficult or impossible to address in ensemble measurements. We first note that even the single particle (F) shows a slight polarization anisotropy that is comparable in magnitude to that

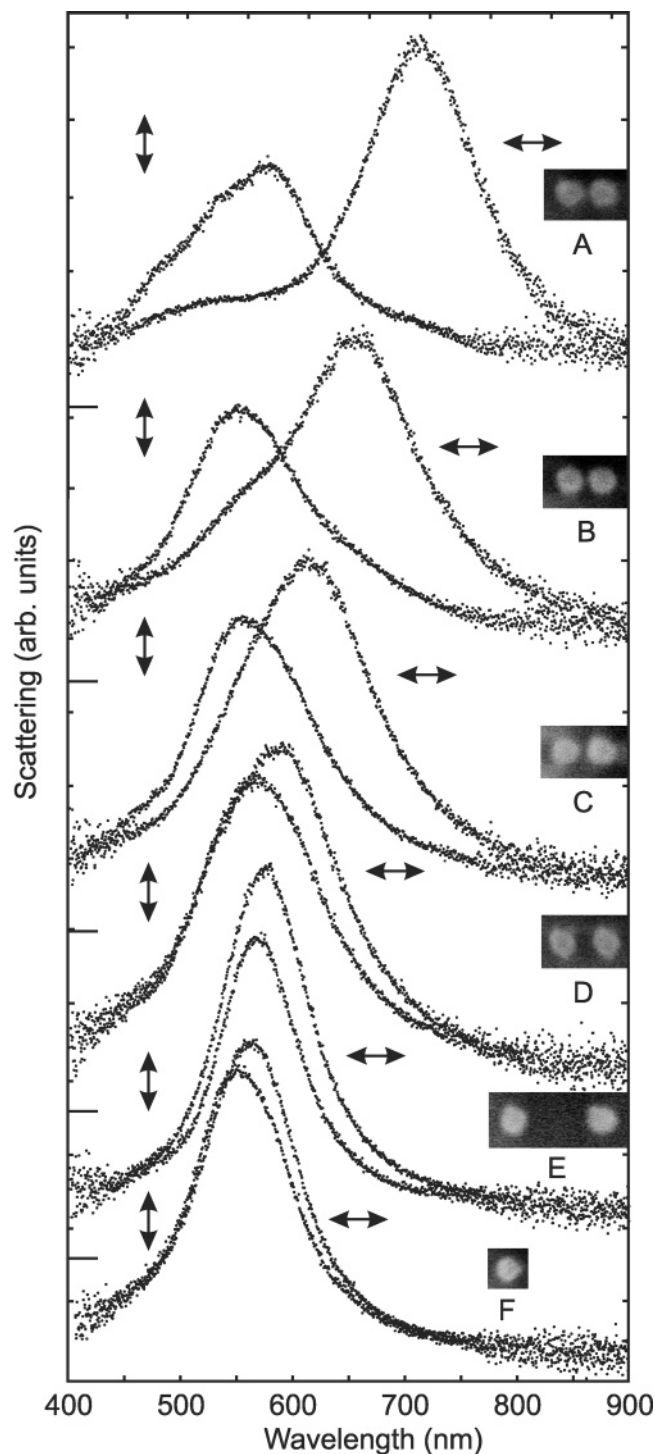


**Figure 6.** Dark-field spectra and SEM micrographs from isolated ( $D = 95$  nm,  $h = 25$  nm) particle pairs with varying separations in parallel and perpendicular polarization, as indicated by arrows. The separations (gaps) between the particles are  $d \approx$  (A) 10, (B) 15, (C) 25, (D) 50, and (E) 250 nm. Spectrum F from a single particle is included for comparison. The vertical bars indicate the baselines for the different spectra.

of the pair (E) with the largest separation. This similarity implies that it is quite difficult to resolve the effects of particle interactions in measurements of single pairs with large separations. In such cases, it is then advantageous to integrate over a population of pairs, so that the deviation from perfect circular symmetry in each individual particle is averaged out. For very short gaps, on the other hand, single-pair data are needed, as discussed above. This is illustrated by spectra A–C, which are



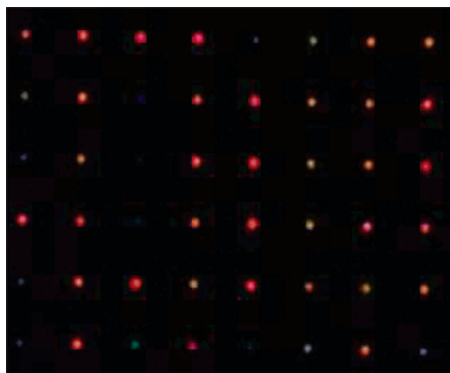


**Figure 7.** Dark-field image of an array of particle pairs (lattice constant =  $5\ \mu\text{m}$ ) in parallel polarization. The pairs are designed to be identical, with a surface separation of approximately 20 nm. However, the spread in actual gap values gives rise to different colors of the pairs.

from pairs designed to have the same separation  $d = 20\ \text{nm}$ . The variation in actual gap size, from  $d \approx 10\ \text{nm}$  in A to  $25\ \text{nm}$  in C, results in a difference in LSP position for the parallel case of approximately 100 nm! We also note that the line width of the long-wavelength peak in A is comparable to the width of single-particle LSPs with similar resonance positions, such as the  $D = 150\ \text{nm}$  particle in Figure 3a. This indicates that the particle interaction as such has little effect on the LSP decay compared to the retardation and electron scattering effects responsible for the line widths of single-particle LSPs.

The spread in the optical properties of particle pairs designed to be “identical” is also illustrated in the dark-field image in Figure 7, which shows an array with a grating constant of  $5\ \mu\text{m}$  in parallel polarization. The pairs ( $D \approx 95\ \text{nm}$ ) in this array were designed to have a gap of 20 nm. In reality, however, the exact separation varies from touching particles (similar to the pair in Figure 5c) to separated particles, with gaps between 10 and 25 nm. These differences result in the different colors seen in the dark-field image, ranging from bright red for closely spaced particles to yellow and even green for larger separations. The very weak blue spots originate from particles connected via a bridge similar to that in Figure 5c. In these cases, the LSPs corresponding to parallel polarization have shifted to the near-infrared region, i.e., outside the sensitivity range of the digital camera or the naked eye. For the perpendicular polarization (not shown), all pairs in the array have more or less the same greenish color.

In Figure 8a, we summarize the pair data for the three investigated particle diameters, combining single-pair measurements for short distances and array data for the larger gap sizes. The combined results clearly confirm the trends already seen in Figure 4, i.e., a red shift that increases with particle size and seems to diverge when the particles are close to metallic contact.

In ref 27, Su et al. presented DDA results that indicate that the relative red shifts (i.e., the peak shifts normalized to the single-particle peak positions) exhibit a universal trend when plotted against the ratio between the gap value and the particle diameter. In Figure 8b, we show that the experimental pair data presented here indeed exhibits such a scaling behavior. The combined data set can be fitted well by an exponential function  $a \exp(-x/b)$ , where  $x = d/D$  is the scaling parameter. The fitting constants  $a \approx 0.37$  and  $b \approx 0.22$  determine the maximum peak shift and the decay of the interparticle interaction with separation.

**4.4. Scattering from Nonseparated Particles.** As illustrated in Figure 7, the parallel-polarization LSP for particles in contact is shifted to the near-infrared range, i.e., much more than any

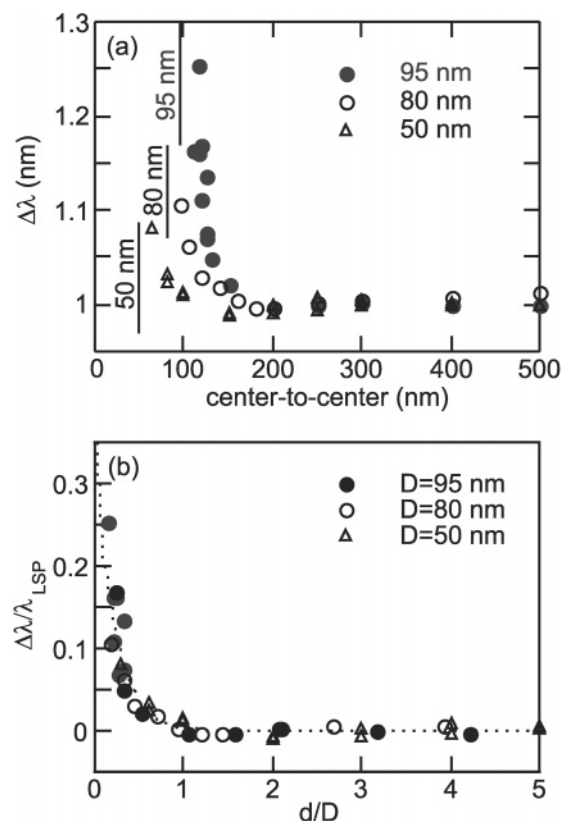


**Figure 8.** (a) Peak shift vs center-to-center distance for the three particle diameters investigated in this work. Single-pair and array data have been combined. (b) Same data as in a replotted as relative peak shift ( $\Delta\lambda/\lambda$ ) vs gap-to-diameter ratio. The dashed line is fit of the experimental data to an exponential decay function.

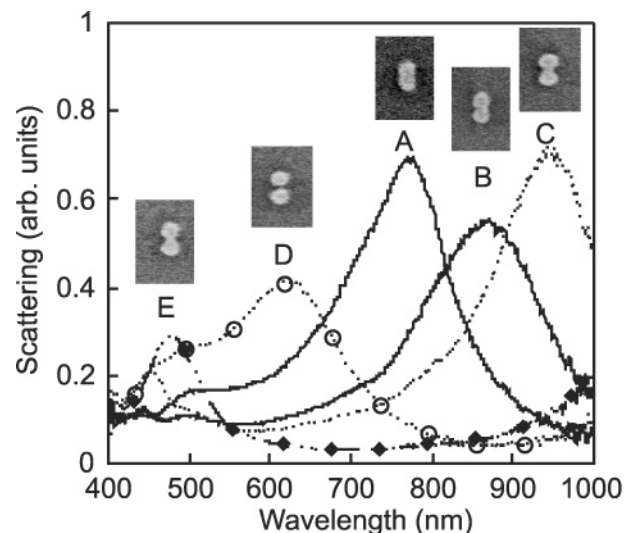


**Figure 9.** Scattering spectra in the parallel polarization geometry from arrays of  $D = 80\ \text{nm}$  and  $h = 40\ \text{nm}$  particle pairs. Spectra A–C and E are from pairs connected by a metallic bridge, whereas spectrum D is from pairs with well-defined gaps.

particle pairs with an experimentally confirmed gap. This raises the question of whether there is an abrupt shift in the LSP position when metallic contact is formed or whether a continuous shift occurs, as argued in ref 26. In Figure 9, we show scattering spectra that address this issue. The data are obtained from ensembles of approximately 10 pairs or intergrown ( $D = 80\ \text{nm}$ ,  $h = 40\ \text{nm}$ ) particles designed to have center-to-center distances between 80 and 110 nm. All samples are greenish in perpendicular polarization, similar to a single  $D = 80\ \text{nm}$  particle

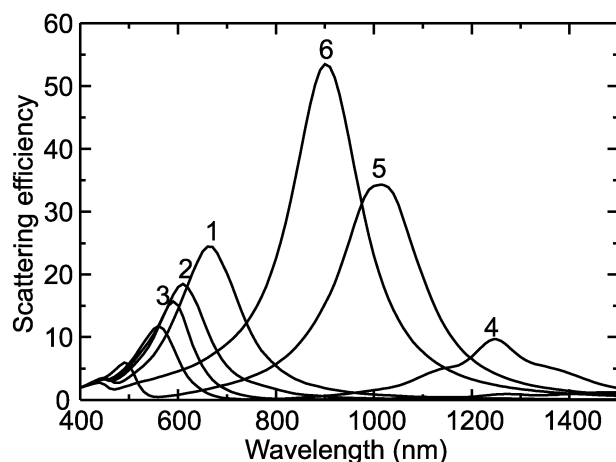


**Figure 10.** Calculated extinction spectra (from DDA calculations) for two disks (95 nm in diameter, 25 nm in height, and 10 nm in spacing) that are linked by a bridge of variable thickness. The bridge consists of a layer of silver that is parallel to the plane of the disks and has a thickness specified in terms of layers that are 1.67 nm thick as follows: 1, no bridge; 2, one layer; 3, two layers; 4, three layers; 5, seven layers; 6, 15 layers (completely filled).

( $\lambda_{\text{LSP}} \approx 515$  nm). Spectra A–C are from particles for which SEM analysis revealed a metallic waist. The total lengths ( $2D + d$ ) of these particles increase from approximately 160 nm in A, to 170 nm in B, to 180 nm in C. It is clear that the corresponding LSPs observed for parallel polarization shift rapidly toward the infrared. The shift is approximately linear with the total length and is in good agreement with previous results for ellipsoidal particles reported by Krenn et al.<sup>47</sup> Obviously, the “hour-glass” shapes of the particles in Figure 9 do not significantly affect the position of the dipolar LSP compared to an ellipsoidal particle with similar total length. One also notes a weaker peak in the 450–500 nm range that increases in magnitude and gradually red shifts with increasing total length. We assign this peak to a quadrupolar mode, in line with the results of ref 47. In fact, it is this quadrupolar resonance that gives rise to the bluish color seen in Figure 7 for intergrown particles.

Spectra E and D in Figure 9 stem from two different areas in the same array designed to have gaps of  $d = 30$  nm, i.e., a total length of 190 nm. This array had a clearly inhomogeneous color, just as in Figure 7, reflecting the spread in separations of different pairs. Areas with mostly brilliant reddish points and areas dominated by weak greenish points could be easily identified. Spectrum E was taken from a greenish area, where the particles are in contact, whereas spectrum D was taken from a reddish area, where the particles were clearly separated. In the first case (E), the dipolar peak is shifted outside the measurement range ( $<1000$  nm), while the quadrupolar peak has grown and has a maximum at approximately 500 nm. The spectral peak positions follow the trends indicated by the intergrown particles with shorter total length (A–C). In contrast, spectrum D peaks at around 620 nm, i.e., the shift compared to the single-particle LSP is in agreement with the behavior discussed in the previous paragraph.

To determine whether the shift from spectrum D to the other spectra is continuous, we performed theoretical calculations on a model system that is designed to investigate the effect of bridging the gap between two particles. The model starts with two 95-nm diameter disks, 25 nm in height, with 10-nm spacing. This matches one of the data sets presented in Figure 4, and the calculated extinction spectrum (curve 1 of Figure 10) peaks at 665 nm.

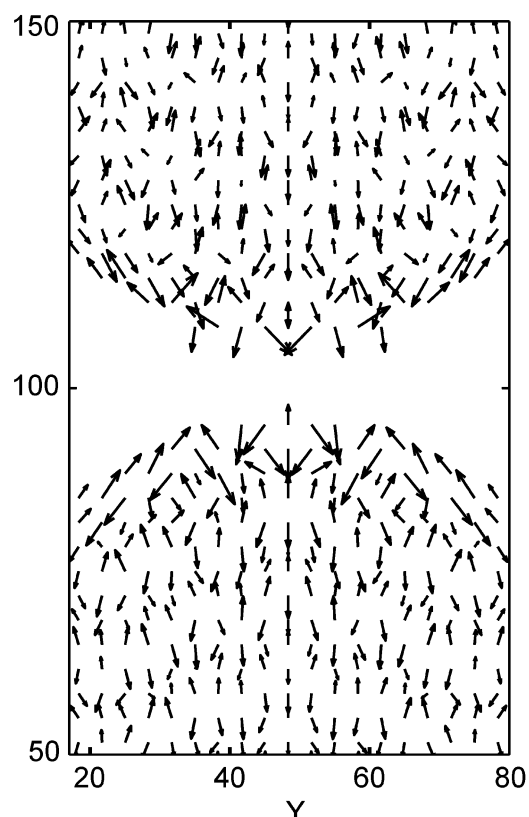


**Figure 11.** Induced polarization for the separated-particle model (curve 1 of Figure 10) corresponding to a wavelength of 665 nm. The DDA calculations were performed with a grid size of 1.67 nm, but only a quarter of the dipoles are shown to enhance visibility. The X and Y axes are in nanometers.

The model then fills in a bridge between the two particles (curves 2–6), starting with a thin sheet (curve 2) and ultimately filling in the entire region between the particles (curve 6). We see that, as the bridge is filled in, the peak at 665 nm gradually blue shifts to 430 nm in curve 6. Meanwhile, a new peak grows in that is initially in the infrared range and blue shifts to 900 nm in curve 6. To assign these features, in Figure 11, we present a plot of the induced polarization in the DDA elements for the separated-particle case in curve 1 at 665 nm. This shows only the region where the particles approach, with the polarization direction taken to be parallel to the interparticle axis. What we see is that the largest polarization vectors are associated with the surfaces of the particles at their point of closest approach. The arrows point (primarily) in opposite directions on the two particles, which is the characteristic feature of a quadrupole mode. From this, we conclude that the peak at 665 nm has strong quadrupolar character, which explains why it correlates to the short-wavelength quadrupole mode in the bridged structure. By contrast, the corresponding polarization plot for the long-wavelength mode (not shown) is primarily dipolar and is primarily localized in the bridge region rather than in the particles (at least until the bridge fills most of the gap).

Comparing Figure 10 with Figure 9, it appears that the transition from peak D (which is very similar to curve 1) to peak A (which is very similar to curve 6) is discontinuous. Evidently, peak D evolves to peak E when the particles are bridged, and the structure that gives rise to peak E also gives rise to a distant dipolar peak at wavelengths longer than 1000 nm. Peaks A–C are clearly dipolar in character, but it seems unlikely that they represent the blue shifting seen in going from curves 4–6 in Figure 10. Instead, because the lengths of the



particles that produce spectra A–C are different, it seems likely that these represent red shifting of the dipolar plasmon as the composite particle lengthens.

The behavior in Figure 11 is similar to what was previously observed by Jensen et al.<sup>35</sup> when particles approach closely. In that work, it was noted that the close proximity of the particles makes it possible for the electric field gradient from dipole excitation of one particle to induce a strong polarization in the other particle that has overall quadrupolar character. In other words, the quadrupolar character in Figure 11 is associated with the electric field gradient being more important than the applied field in determining the induced polarization.

## 5. Summary

We have performed a study of the optical properties of disk-shaped silver particles and pairs of such particles prepared by electron beam lithography, with an emphasis on single objects characterized by electron microscopy. The dipolar localized surface plasmon resonance observed for incident polarization parallel to the pair axis red shifts dramatically when the interparticle distance is decreased. These results agree well with previous reports on pairs of gold particles,<sup>26,27</sup> although the magnitude of the shift is much larger than what was observed before. The particle interaction is most pronounced for surface separations smaller than approximately 30 nm. At these distances, the fabrication process produces a relatively wide spread in the exact separation, which highlights the importance of single-pair data. In particular, we show that metallic contact between particles leads to new plasmon modes that have extremely large shifts relative to the separated-particle frequencies. This effect could easily be misinterpreted as an interparticle interaction in ensemble measurements. The experimental results agree quantitatively with calculations based on coupled point dipoles and with numerical calculations based on the discrete dipole approximation. However, the latter approach gives better agreement for small particle separations.

**Acknowledgment.** We thank Eva Olsson for generous help with the TEM analysis. We acknowledge support of the Swedish Foundation for Strategic Research, the Swedish Research Council, the Nanoscale Science and Engineering Initiative of the National Science Foundation under NSF Award EEC-0118025, and the AFOSR MURI Grant F49620-01-1-0381.

## References and Notes

- (1) Mie, G. *Ann. Phys. (Leipzig)* **1908**, 25, 377–445.
- (2) Shipway, A. N.; Katz, E.; Willer, I. *ChemPhysChem* **2000**, 1, 18–52.
- (3) Bohren, C. F.; Huffman, D. R. *Absorption and Scattering of Light by Small Particles*; Wiley: New York, 1983.
- (4) Kreibig, U.; Vollmer, M. *Optical Properties of Metal Clusters*; Springer, New York, 1995.
- (5) Kelly, K. L.; Coronado, E.; Zhao, L.; Schatz, G. C. *J. Phys. Chem. B* **2003**, 107, 668–677.
- (6) Moskovits, M. *Rev. Mod. Phys.* **1985**, 57 (3), 783–826.
- (7) Schatz, G. C.; Van Duyne, R. P. In *Handbook of Vibrational Spectroscopy*; Chalmers, J. M., Griffiths, P. R., Eds.; Wiley: New York, 2001; pp 759–774.
- (8) Maier, S. A.; Kik, P. G.; Atwater, H. A.; Meltzer, S.; Harel, E.; Koel, B. C.; Requicha, A. R. G. *Nature Mater.* **2003**, 2, 229–232.
- (9) Quinten, M.; Leitner, A.; Krenn, J. R.; Aussenegg, F. R. *Opt. Lett.* **1998**, 23 (17), 1331–1333.
- (10) Storhoff, J. J.; Elghanian, R.; Mucic, R. C.; Mirkin, C. A.; Leitsinger, R. L. *J. Am. Chem. Soc.* **1998**, 120, 1959–1964.
- (11) McFarland, A. D.; Van Duyne, R. P. *Nano Lett.* **2003**, 3, 1057–1062.
- (12) Olofsson, L.; Rindzevicius, T.; Pfeiffer, I.; Käll, M.; Höök, F. *Langmuir* **2003**, 19, 10414–10419.
- (13) Haes, A.; Duyne, R. P. V. *J. Am. Chem. Soc.* **2002**, 124, 10596–10604.
- (14) Lamprecht, B.; Schider, G.; Lechner, R. T.; Krenn, J. R.; Aussenegg, F. R. *Phys. Rev. Lett.* **2000**, 84, 4721–4724.
- (15) Haynes, C. L.; McFarland, A. D.; Zhao, L. L.; Van Duyne, R. P.; Schatz, G. C.; Gunnarsson, L.; Prikulis, J.; Kasemo, B.; Käll, M. *J. Phys. Chem. B* **2003**, 107, 7337–7342.
- (16) Gotschy, W.; Vonmetz, K.; Leitner, A.; Aussenegg, F. R. *Appl. Phys. B* **1996**, 63, 381–384.
- (17) Kahl, M.; Voges, E. *Phys. Rev. B* **2000**, 61 (20), 14078–14088.
- (18) Jensen, T. R.; Malinsky, M. D.; Haynes, C. L.; Van Duyne, R. P. *J. Phys. Chem. B* **2000**, 104, 10545–10556.
- (19) Meier, M.; Wokaun, A.; Liao, P. F. *J. Opt. Soc. Am. B* **1985**, 2, 931–949.
- (20) Zhao, L. L.; Kelly, K. L.; Schatz, G. C. *J. Phys. Chem. B* **2003**, 107, 7343–7350.
- (21) Kneipp, K.; Wang, Y.; Kneipp, H.; Perelman, L. T.; Itzkan, I.; Dasari, R. R.; Feld, M. S. *Phys. Rev. Lett.* **1997**, 78, 1667–1670.
- (22) Nie, S.; Emory, S. R. *Science* **1997**, 275, 1102–1106.
- (23) Xu, H.; Bjerneld, J.; Käll, M.; Börjesson, L. *Phys. Rev. Lett.* **1999**, 83, 4357–4360.
- (24) Jiang, J.; Bosnick, K.; Milliard, M.; Brus, L. *J. Phys. Chem. B* **2003**, 107, 9964–9972.
- (25) Xu, H.; Käll, M. *Phys. Rev. Lett.* **2002**, 89, 246802.
- (26) Rechenberger, W.; Hohenau, A.; Leitner, A.; Krenn, J. R.; Lamprecht, B.; Aussenegg, F. R. *Opt. Commun.* **2003**, 220, 137–141.
- (27) Su, K. H.; Wei, Q. H.; Zhang, X.; Mock, J. J.; Smith, D. R.; Schultz, S. *Nano Lett.* **2003**, 3, 1087–1090.
- (28) Tamaru, H.; Kuwata, H.; Miyazaki, H. T.; Miyano, K. *Appl. Phys. Lett.* **2002**, 80, 1826–1828.
- (29) Prikulis, J.; Svedberg, F.; Käll, M.; Enger, J.; Ramser, K.; Goksör, M.; Hanstorp, D. *Nano Lett.* **2004**, 4, 115–118.
- (30) Tennant, D.; Fullowan, R.; Taemura, H.; Isobe, M.; Nakagawa, Y. *J. Vac. Sci. Technol. B* **2000**, 18, 3089–3094.
- (31) Eidelloth, W.; Sandstrom, R. L. *Appl. Phys. Lett.* **1991**, 59, 1632–1634.
- (32) Vieu, C.; Carcenac, F.; Pepin, A.; Chen, Y.; Mejjias, M.; Lebib, A.; Manin-Ferlazzo, L.; Couraud, L.; Launois, H. *Appl. Surf. Sci.* **2000**, 164, 111–117.
- (33) Broers, A. N.; Hoole, A. C. F.; Ryan, J. M. *Microelectron. Eng.* **1996**, 32, 131–142.
- (34) Grant, A. W.; Hu, Q. H.; Kasemo, B., in preparation.
- (35) Jensen, T.; Kelly, L.; Lazarides, A.; Schatz, G. C. *J. Cluster Sci.* **1999**, 10, 295–317.
- (36) Devoe, H. J. *Chem. Phys.* **1964**, 41 (2), 393.
- (37) Devoe, H. J. *Chem. Phys.* **1965**, 43 (9), 3199.
- (38) Purcell, E. M.; Pennypacker, C. *Astrophys. J.* **1973**, 186 (2), 705.
- (39) Draine, B. T. *Astrophys. J.* **1988**, 333 (2), 848.
- (40) Draine, B. T.; Flatau, P. J. *J. Opt. Soc. Am.* **1994**, 11 (4), 1491.
- (41) Draine, B. T.; Goodman, J. J. *Astrophys. J.* **1993**, 405, 685.
- (42) Malinsky, M. D.; Kelly, K. L.; Schatz, G. C.; VanDuyne, R. P. *J. Phys. Chem. B* **2001**, 105, 2343–2350.
- (43) Zou, S.; Zhou, L.; Schatz, G. C. *SPIE Proc.* **2003**, 5221, 174–181.
- (44) Hanarp, P.; Käll, M.; Sutherland, D. J. *J. Phys. Chem. B* **2003**, 107, 5768–5772.
- (45) Haynes, C. L.; VanDuyne, R. P. *J. Phys. Chem. B* **2001**, 105, 5599–5611.
- (46) Liu, K.; Avouris, P.; Bucchignano, J.; Martel, R.; Sun, S.; Michl, J. *Appl. Phys. Lett.* **2002**, 80, 865–867.
- (47) Krenn, J. R.; Schider, G.; Rechenberger, W.; Lamprecht, B.; Leitner, A.; Aussenegg, F. R.; Weeber, J. C. *Appl. Phys. Lett.* **2000**, 77, 3379–3381.